Systematic calibration of a 2-m Ring Solar Telescope based on local interferometry and model comparison (postprint)

Authors: Renai Liu, Jinpeng Li, Zuozifei Song, Changyu Zeng, Yichun Dai, Zuo Zifei Song

Date: 2025-06-03T15:41:55+00:00

Abstract

To address the installation challenges of a 2-m ring Gregorian telescope system and similar optical systems with a small width-to-radius ratio, we propose a detection method combining local interferometry with a comparison model. This method enhances the precision of system calibration by establishing a dataset delineating the relationship between secondary mirror misalignment and wavefront aberration, subsequently inferring the misalignment from interferometric detection results during the calibration process. For the 2-m ring telescope, we develop a detection model employing five local sub-apertures, enabling a root-mean-square detection accuracy of 0.0225λ ($\lambda = 632.8$ nm) for full-aperture wavefront aberration. Calibration results for the 2-m Ring Solar Telescope system indicate that the root-mean-square value of sub-aperture wavefront aberration reaches 0.104λ, and the root-mean-square value of stitched full-aperture measurement results reaches 0.112λ. This method provides a novel approach for calibrating small width-to-radius ratio telescope systems and can be applied to the calibration of other irregular-aperture optical systems.

Full Text

Preamble

Astronomical Techniques and Instruments, Vol. 2, May 2025, 175–185

Article Open Access

Systematic Calibration of a 2-m Ring Solar Telescope Based on Local Interferometry and Model Comparison

Renai Liu[1],[2], Jinpeng Li[1],[4],[5]*, Zuozifei Song[1],[2], Changyu Zeng[1],[2], Yichun Dai[3]

[1]Nanjing Astronomical Instrument Research and Development Center, Chinese Academy of Sciences, Nanjing 210042, China
[2]School of Astronomy and Space Science, University of Science and Technology of China, Hefei 230026, China
[3]Yunnan Observatories, Chinese Academy of Sciences, Kunming 650216, China
[4]Nanjing Astronomical Instruments Co., LTD, Chinese Academy of Sciences, Nanjing 210042, China
[5]Purple Mountain Observatory, Chinese Academy of Sciences, Nanjing 210023, China

*Correspondence: 20240139@njupt.edu.cn

Received: November 4, 2024; **Accepted:** January 27, 2025; **Published Online:** March 26, 2025
https://doi.org/10.61977/ati2024061; **https://cstr.cn/32083.14.ati2024061**

Citation: Liu, R. A., Li, J. P., Song, Z. Z. F., et al. 2025. Systematic calibration of a 2-m Ring Solar Telescope based on local interferometry and model comparison. *Astronomical Techniques and Instruments*, 2(3): 175−185. https://doi.org/10.61977/ati2024061.

Abstract: To address the installation challenges of a 2-m ring Gregorian telescope system, and similar optical systems with a small width-to-radius ratio, we propose a detection method combining local interferometry with a comparison model. This method enhances the precision of system calibration by establishing a dataset that delineates the relationship between secondary mirror misalignment and wavefront aberration, subsequently inferring the misalignment from interferometric detection results during the calibration process. For the 2-m ring telescope, we develop a detection model using five local sub-apertures, enabling a root-mean-square detection accuracy of 0.0225λ ($\lambda = 632.8$ nm) for full-aperture wavefront aberration. The calibration results for the 2-m Ring Solar Telescope system indicate that the root-mean-square value of sub-aperture wavefront aberration reaches 0.104λ, and the root-mean-square value of spliced full-aperture measurement yields 0.112λ. This method offers a novel approach for calibrating small width-to-radius ratio telescope systems and can be applied to the calibration of other irregular-aperture optical systems.

Keywords: Local aperture; Model comparison; 2-m Ring Solar Telescope; System calibration; Splicing algorithm

1. Introduction

The advancement of modern astronomy has precipitated a growing demand for telescopes with enhanced observational precision, necessitating improvements in resolving power. There are two main approaches to augmenting the resolving power of telescopes. The first involves employing synthetic aperture technology to enhance spatial resolution, but this technology requires further development in the visible and near-infrared wavelength ranges. The second approach is to increase the diameter of the telescope, because a larger aperture can significantly enhance spatial resolution capabilities and improve observable details [?, ?]. By observing the magnetic structures and evolutionary processes of the solar atmosphere at high resolution, large-aperture solar telescopes can elucidate fundamental physical processes, such as the mechanisms underlying coronal heating and the generation and enhancement of stellar magnetic fields. These observations not only furnish experimental data and theoretical support for various high-energy disciplines, including plasma physics, physics, and atomic physics, but also offer critical insights for the further study of stars, galaxies, and the interstellar medium \cite{3–6}.

At present, the predominant configurations of ground-based solar telescopes are categorized as open-type and vacuum-type \cite{7–9}. A notable example of open-type telescopes is the Daniel K. Inouye Solar Telescope (DKIST) located in Maui, Hawaii, with an off-axis Gregorian design [?]. The 1 m New Vacuum Solar Telescope (NVST) at Yunnan Observatories, CAS, in China exemplifies vacuum telescope technology and employs an enhanced Gregorian configuration [?]. While off-axis systems facilitate the thermal control of the hot stop, they also introduce more significant polarization interference. Conversely, circular aperture designs offer superior optical symmetry, thereby enhancing high-precision polarization measurements. Additionally, when such systems exhibit a small width-to-radius ratio, their thermal control design remains relatively straightforward. Consequently, a new generation of solar telescope designs, incorporating circular apertures, has been proposed [?].

For telescope systems with circular or irregularly shaped apertures, precise alignment is essential to achieve optimal imaging performance. As the aperture size of the telescope increases and the width-to-radius ratio diminishes, it poses greater challenges associated with calibration and inspection of the system. Currently, calibration technologies for large-aperture telescopes include laser tracker positioning technology, Shack-Hartmann wavefront sensing technology, star testing methods, and pentaprism scanning inspections. Cao et al. used a laser tracker to achieve precision calibration of the new 1.6 m solar telescope at the Great Bear Observatory [?], and shortly afterward, Li et al. used Shack-Hartmann wavefront sensing technology to successfully detect the wave aberration of a large-aperture telescope system with a diameter of 1 m and a focal length of 11 m [?]. Li et al. proposed an active alignment method for astronomical telescopes based on the ellipticity of multi-field star images to calibrate the AST3-3 South Pole Survey telescope [?]. An et al., at the Changchun Institute of Optics, Fine

Mechanics and Physics, CAS, proposed the use of an optical fiber-connected photon scanning pentaprism for the alignment measurement of a large-aperture telescope system [?]. However, these methods have not been used specifically for calibration of ring or special-aperture telescope systems before.

In this context, the width-to-radius ratio of a 2-m ring ground-based solar telescope is relatively small, leading to a significant reduction in effective data available for detection. Consequently, conventional calibration methods provide inadequate accuracy. To address this issue, we employ a local aperture standard flat mirror to assess the large-aperture optical system characterized by a small width-to-radius ratio by evaluating the minor ratios of both main and auxiliary mirrors. By establishing a correlation between secondary mirror misalignment and wavefront aberration within the system, we can invert misalignment based on actual interferometric detection results to achieve precise calibration. This study presents an innovative approach for calibrating aberration-corrected dual-reflection optical systems with atypically shaped apertures. The term "atypically shaped apertures" here refers to shapes other than the traditional circular ones, such as the small width-to-radius ratio annular aperture in this paper, the crescent-shaped sub-aperture utilized for measurements, and other irregular apertures resulting from obscuration within the optical system. It has the advantage of being applicable to the calibration of various types of primary and secondary mirrors and is particularly beneficial for small width-to-radius ratio telescope systems, which are challenging to calibrate using traditional techniques.

2. 2-m Ring Ground-Based Solar Telescope System and Calibration Method

2.1. 2-m Ring Ground-Based Solar Telescope System

The 2-meter Ring Solar Telescope (2mRST) employs a horizontal Gregorian optical configuration, comprising a primary mirror M1 and a secondary mirror M2, as shown in Fig. 1 [FIGURE:1]. A hot stop is implemented at the first focal point (F1) of the system [?], to mitigate the thermal load in this location [?], and the rear optical path [?] is provided at the secondary focal point (F2) of the system.

Owing to its novel design, the 2mRST system attains nearly diffraction-limited optical transfer functions across all fields of view, ensuring excellent overall imaging quality and enabling high-resolution observations of the intricate structures within the solar photosphere, chromosphere, and corona in terms of spatial, temporal, spectral, and magnetic dimensions [?].

The design of the 2mRST includes a banded structure with a relatively small width-to-radius ratio for the main mirror of the system. The outer diameter of the main mirror is 2000 mm, the bandwidth is 350 mm, and the width-to-radius ratio of the mirror is 0.35. This design is based on two considerations. Firstly, the banded structure facilitates the setting of the focus. At the same time, the ring symmetrical structure with a smaller width-to-radius ratio can effectively eliminate the crosstalk among the polarization states of light waves, which is conducive to high-precision magnetic field detection and inversion. Compared with large telescopes of the same resolution, the ring solar telescope is lightweight, has low wind resistance, and uses a relatively simple frame structure [**?**].

Despite the aforementioned advantages of the 2mRST design, its practical application in large-aperture telescopes has been limited because of its unique geometric configuration, which poses significant challenges for aligning both primary and secondary mirrors. Typically, alignment within a two-reflector system is achieved through interferometric autocollimation. However, this approach presents certain limitations when applied to the 2mRST design. Specifically, constraints related to the diameter of standard flat mirrors used for full-aperture detection in the 2mRST system, coupled with the small width-to-radius ratio inherent to its ring structure, result in a reduction of effective measurement data by approximately 62.34%. Furthermore, insufficient data from the central region of the measured system severely compromises the orthogonality of Zernike polynomial coefficients derived from commercial interferometers. Consequently, there is an urgent need for a new system detection method to facilitate proper alignment.

2.2. Small Width-to-Radius Ratio Ring Optical System Calibration Method

To solve the problems mentioned in the previous section, we present a novel method for the calibration system of local aperture measurement via model comparison. Local aperture measurement is carried out using a standard flat mirror with a smaller aperture, with the local aperture defined as shown in Fig. 2 [FIGURE:2].

By using optical design software in accordance with the actual parameters of each optical element, such as the optical curvature radius, aspheric coefficient, aperture, and shape, we construct a detection optical path model (shown in Fig. 3A

). During the detection process, an optical path equivalent to the detection optical path model is set up. The light path trajectory of the self-collimation is as follows: The spherical wave emitted by the interferometer is reflected by the secondary mirror and incident on the primary mirror. It is then reflected by the primary mirror and incident on the standard flat mirror with a smaller aperture, before being self-collimated back to the interferometer by the small-aperture flat mirror. Finally, the system wave aberration is detected by the interferometer. Due to the influence of the small-aperture flat mirror and the wide width-to-radius ratio, the data obtained by the interferometer is the system wave aberration of the local aperture. Since the system wave aberration obtained in the optical design software is equivalent to that directly detected

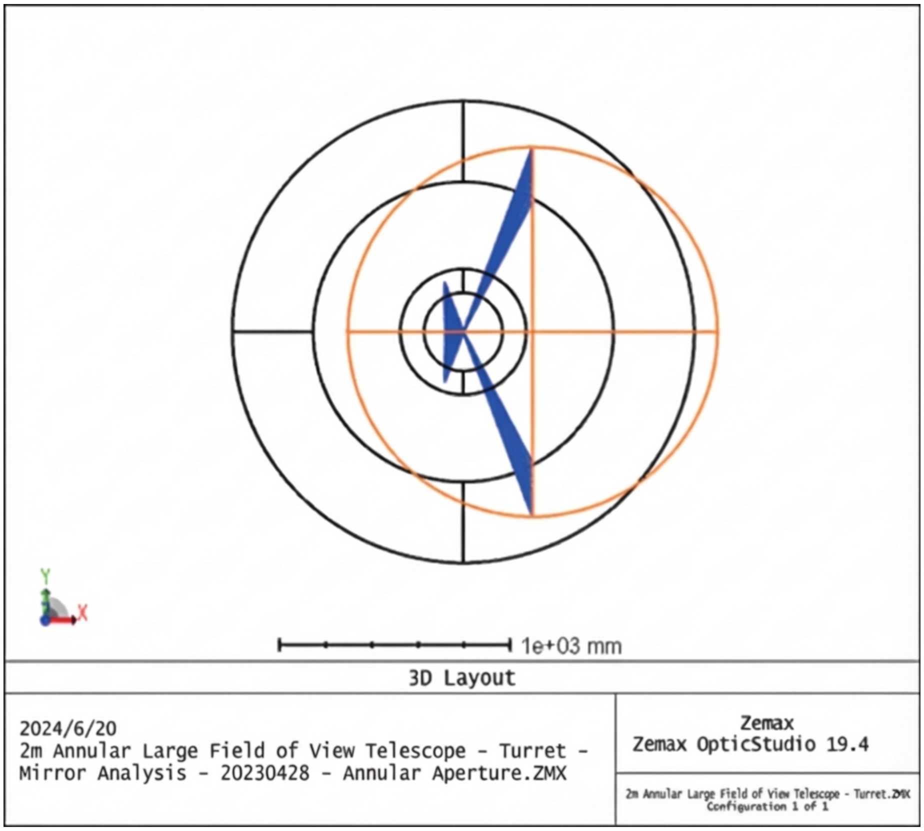

Figure 1: Figure 3

by the interferometer, the misalignment between the primary and secondary mirrors can be evaluated by comparing the system wave aberration of the local aperture first, thereby guiding calibration.

In our detection model, we analyze the system wave aberrations under five local aperture conditions (shown in Fig. 2). Considering the misalignment of the secondary mirror, including decentration, tilt, and defocus, we find the numerical relationship between the wave aberration of the local area of the system and the misalignment quantity as WVi(D;T;P;L) for i=1,2,3,4,5, where D is the decentration of the secondary mirror in the model, T is the tilt of the secondary mirror in the model, P is the defocus of the secondary mirror in the model, and L is the offset of the standard flat mirror in the model. The data set for the relationship between the misalignment quantity and the system wave aberration is established as fD;T;P;Lg. In the actual measurement, we conduct local aperture measurements equivalent to the model. The local aperture system wave aberration obtained by the interferometer is WRi(d;t;p;l) for i=1,2,3,4,5, where d is the decentration of the secondary mirror in the actual detection, t is the tilt of the secondary mirror in the actual detection, p is the defocus of the secondary mirror in the actual detection, and l is the offset of the standard flat mirror in the actual detection.

The relationship between the misalignment of the secondary mirror, the wave aberration of the local aperture area actually collected, and the local aperture wave aberration at the corresponding position in the calibration model is given by (d;t;p)=FIND(WVi;WRi), where "FIND" is the similarity comparison between WVi and WRi. One method of similarity comparison is to calculate the correlation of the images; the other is to analyze the distribution characteristics of the wavefront aberration at different areas in the system and evaluate the root mean square (RMS) value. Once the values of d, t and p are obtained, the calibration deviation of the secondary mirror can be found, guiding calibration. Since this calibration cannot be accomplished with a single measurement, multiple calibrations are required. The flowchart for this method is presented in Fig. 3B

.

3. 2mRST System Local Detection Model

Based on the parameters of the optical components presented in Table 1 , we construct a model using the optical design software. Using a local aperture of 1600 mm, we divided the system into five local measurement regions (shown in Fig. 4 [FIGURE:4]). To increase the test area as much as possible, five local test regions were situated at: an offset of 200 mm along the positive X-axis, an offset of 200 mm along the negative X-axis, an offset of 200 mm along the positive Y-axis, an offset of 200 mm along the negative Y-axis, and the center of the system under test.

Table 1. Real parameters of each optical element

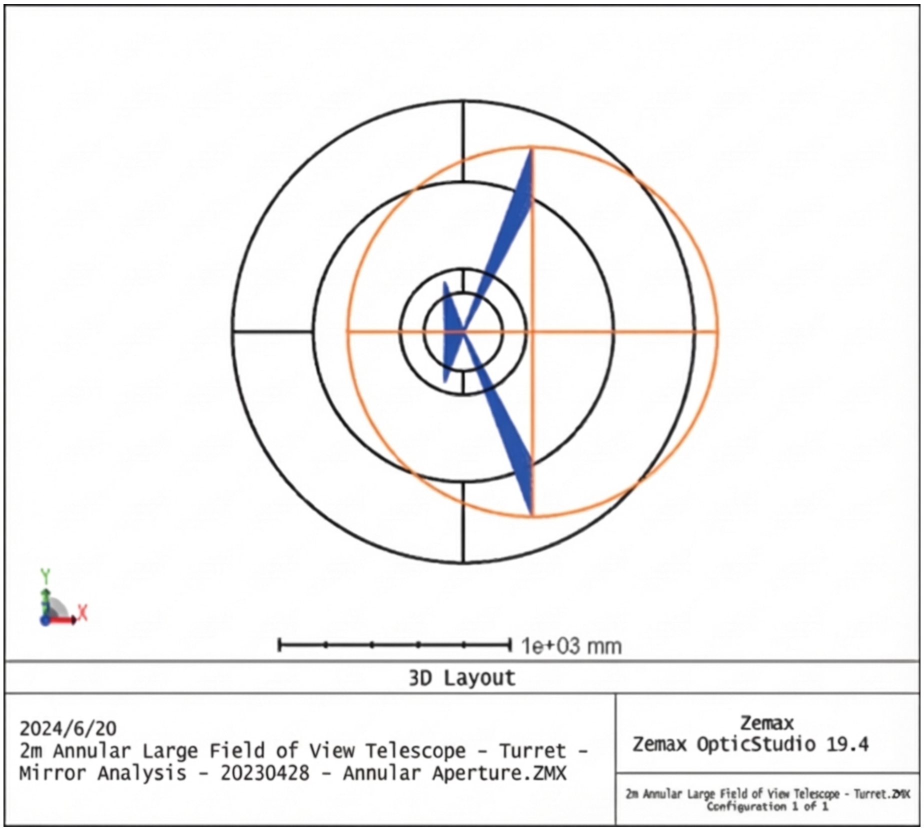

Figure 2: Figure 3

Optical element	Radius of curvature/mm	Conic	Diameter/mm	Aperture
2-m ring primary mirror	-6000	-0.977	2000	Circular
Ring secondary mirror	-2100	-0.437	600	Circular
1.6 m standard flat mirror	Infinity	—	1600	Circular

Taking the primary mirror as the benchmark, we set the misalignment of the secondary mirror in the model to correspond to the actual misalignment of the secondary mirror in different directions during the assembly and adjustment process. The six misalignments of the secondary mirror are translations in the X/Y/Z directions and rotations around the X/Y/Z axes, as shown in Fig. 5 [FIGURE:5]. The light returned from the standard flat mirror self-collimated by the interferometer did not coincide with the reference light within the interferometer, causing the secondary mirror to need some corresponding adjustment to compensate for this misalignment, allowing the interference light and the reference light to converge at a single point. Given that the secondary mirror is a ring-shaped axially symmetric structure, its rotation around the Z-axis does not introduce system wave aberration. Moreover, the Y-axis tilt can compensate for the X-axis decentration of the secondary mirror, the X-axis tilt can compensate for the Y-axis decentration, and the Z-axis defocus can be compensated for using movement of the interferometer in the Z-axis direction (shown in Table 2). Consequently, only the numerical relationships between the system wave aberration and the misalignment in the three cases need to be taken into account: the X-axis decentration of the secondary mirror (compensated by TY), the Y-axis decentration (compensated by TX), and the Z-axis defocus (compensated by DIZ).

Table 2. Relationship between the misalignment of the secondary mirror

Optical parameters	No mutual compensation	Mutual compensation
Decentration X (DX)	—	TY
Decentration Y (DY)	—	TX
Defocus Z (PZ)	—	DIZ

We simulate scenarios in which the secondary mirror has X-axis decentration and Y-axis decentration. The wavefront aberration performances of the five local detection regions and the full aperture of the system to be detected display coma, shown in Fig. 6A [FIGURE:6] and Fig. 6B. In Fig. 6A, the wavefront aberration map of local detection region 1 indicates a low outer ring and a high inner ring, while local detection region 2 shows a high outer ring and a low inner ring. The wavefront aberration map of local detection region 5 reveals a lower left and higher right outer ring and a higher left and lower right inner ring, which is consistent with the trend of the wavefront aberration map of the corresponding local region when there is X-direction coma in the system. Fig. 6B shows the wavefront aberration map of local detection region 3 with a low outer side and a high inner side, while local detection region 4 shows a high outer side and a low inner side. The local detection area 5 shows that the outer circle is higher on the upper side and lower on the lower side, while the inner circle is lower on the upper side and higher on the lower side, which is consistent with the trend of the wavefront aberration map of the corresponding local region when there is Y-direction coma in the system. As shown in Fig. 6C, the wavefront aberration maps of local detection regions 1 and 2 show a high outer ring and a low inner ring, which is consistent with the trend of the wavefront aberration map of the corresponding local regions when there is Z-direction defocus in the system.

Regardless of whether the secondary mirror has decentration or tilt, the wave aberration of this system presents in the form of coma. When a standard planar mirror is placed at the eccentric position for detection, the wave aberration images of the eccentric positions on both sides of the system have a distinct difference in height. However, when the secondary mirror has defocus in the Z-axis direction, regardless of where the planar mirror is placed in the eccentric position, the wave aberration performance of the system remains the same.

The adjustment process initially uses a laser tracker for rough calibration, to control the relative position deviation between the primary and secondary mirrors within a narrow range (measurement accuracy of the laser tracker is presented in Table 3). The distance between the primary and secondary mirrors here is 3820 mm, so the measurement accuracy can reach 26.74 m.

Table 3. Measurement accuracy of the laser tracker

Distance measurement performance	Working range	Resolution	Accuracy (MPE*)
ADM-3D	—	0.5 m	15 m or 0.7 m/m (Whichever is greater

*Maximum permissible errors

Volumetric accuracy (MPE) | 15 m + 5 m/m |
Precision level accuracy | — |

The simulation of the misalignment range of the secondary mirror, relative to the primary mirror within 0.01–10 mm, incorporates the adjustment range of the secondary mirror, human operation errors, and environmental disturbances, in the optical design software. The numerical relationship between the wave aberration measured in the local area and the misalignment is shown in Fig. 7 [FIGURE:7], and the numerical relationship between the wave aberration measured in the full aperture and the misalignment is also presented.

Using the database of the system wavefront aberration RMS and the misalignment of the secondary mirror established above, we find that under the same misalignment amount, the RMS sensitivity of the system wavefront aberration is lowest during centering measurements. Therefore, we use a standard flat mirror to first perform centering detection and then off-center detection. When the RMS of the local wavefront aberration of the system is measured as 0.827λ ($\lambda = 632.8$ nm), the RMS of the full-aperture wavefront aberration can reach 0.0225λ.

4. 2mRST System Local Detection Model Establishment

We perform our calibration experiment on the 2mRST system according to our established model. Fig. 8A [FIGURE:8] presents the coordinate axes of the system, where point A is the central point on one side of the circumference where the inner wall of the primary mirror intersects with the end face. With the center point of the end face of the primary mirror as the origin O, the optical axis of the system as the Z-axis, and the straight-line OA as the X-axis. We measure the misalignment of the secondary mirror relative to the primary mirror using a laser tracker for the rough calibration of the system (a photograph of the equipment is shown in Fig. 8B [FIGURE:8]).

Table 4. Relative initial positions of the primary and secondary mirrors

Secondary mirror center relative to the origin	Eccentric/mm	Tilt/(°)
X-axis	-1.17	0.184
Y-axis	-0.2215	0

For fine calibration, we constructed a self-collimation optical path. The entire self-collimation interferometric detection optical path consists of a 2-m-aperture ring primary mirror, a ring secondary mirror, a 1.6-m-aperture standard planar mirror, and a 632.8-nm laser interferometer (shown in Fig. 9 [FIGURE:9]).

When there is a misalignment in the secondary mirror and a standard flat mirror offset l = 0 mm, the local wavefront aberration measured by the interferometer is compared with the system wavefront aberration database, WVi(D;T;P;L) for i=1,2,3,4,5, established in Section 2 through model comparison. Thus, the deviation value (d;t;p) that the secondary mirror needs to adjust is calculated using Equation (1). The initial system wavefront aberration manifests as coma, which reveals a considerable relative decentration between the primary and secondary mirrors. The interferometer acquires extremely fine interference fringes (shown in Fig. 10A [FIGURE:10]). The RMS of the measured wavefront aberration (WR5) is 0.8248λ ($\lambda = 632.8$ nm), as shown in Fig. 10B. Due to the influence of the airflow mass above the primary mirror, the system wavefront aberration (WV5) is 0.233λ, as shown in Fig. 10C. The status of the secondary mirror is DX = 1.255 mm, DY = -1.8 mm, TX = 0.076568°, TY = 0.053385°.

After multiple adjustments of the deviation value of the secondary mirror, when the standard flat mirror was positioned at l = 0 mm, and the measured RMS of the system wavefront aberration is shown in Fig. 10D. The fringes measured by the interferometer are clearly distinguishable, as shown in Fig. 10E. The RMS of the measured wavefront aberration (WR5) is 0.771λ ($\lambda = 632.8$ nm), as shown in Fig. 10F. The system wavefront aberration causes astigmatism, mainly induced by the support structure of the telescope system and the temperature stratification of the large-aperture surface of the main mirror.

When the offset l of the standard flat mirror is 200 mm, the system interference fringes are shown in Fig. 11A [FIGURE:11]. The RMS of the measured wavefront aberration (WR1) is 0.541λ ($\lambda = 632.8$ nm), as shown in Fig. 11B, and the RMS of the wavefront aberration (WV1) in the calibration model is 0.5476λ ($\lambda = 632.8$ nm), as shown in Fig. 11C.

When l = -200 mm for the standard flat mirror, interference fringes occur, as shown in Fig. 11D. The RMS of wavefront aberration measured is 0.543λ ($\lambda = 632.8$ nm), as shown in Fig. 11E, and the RMS of the wavefront aberration in the calibration model is 0.5437λ ($\lambda = 632.8$ nm), as shown in Fig. 11F.

The wavefront aberration of the system predominantly causes coma, resulting from the tilting of the primary and secondary mirrors. The concurrent status of the secondary mirror is DX = 0.87 mm, TX = 0.03705°.

After multiple adjustments of the position of the secondary mirror, when the standard flat mirror is at l = 200 mm, the results of the measured wavefront aberration of the system are shown in Fig. 12A [FIGURE:12]. The measured experimental results from the calibration experiment indicate that when the standard flat mirror is at l = -200 mm, the PV and RMS of the wavefront aberration of the optical system under test are 5.523λ and 0.541λ respectively, as shown in Fig. 12B, with wavefront aberration causing astigmatism. This comes from the surface shapes of the primary and secondary mirrors and the mirror support structures.

When l = 200 mm for the standard flat mirror, the PV and RMS of the wavefront aberration are 4.935λ and 0.786λ respectively, completing the calibration, as shown in Fig. 12C, with wavefront aberration causing astigmatism. This comes from the surface shapes of the primary and secondary mirrors, the mechanical support structure of the system, and temperature stratification in the local environment.

5. Discussion

In contrast to traditional two-reflector systems, the alignment of small width-to-radius ratio ring optical systems mainly presents two challenges: A smaller width-to-radius ratio will lead to a reduction in the amount of effective measurement data, while the relatively small radius of the standard flat mirror compared to the overall system will also cause a decrease in effective measurement data.

This section takes into account the system calibration accuracy of the above two factors and analyzes the application scope of our proposed method.

Currently, the RMS accuracy of the wavefront aberration of commercial interferometers is 0.01λ. The filling factor of a local area is defined as the proportion of the area of the standard flat mirror to the total light-receiving area of the system, denoted by $t = (\pi r^2)/(\pi R^2)$. As shown in Fig. 14

Figure 3: Figure 14

, when the standard flat mirror L is coaxial with the optical system and the optical system has a misalignment, the detection results of a given commercial interferometer under a different filling factor t and a different width-to-radius ratio RWR can be simulated using optical design software.

With the same amount of misalignment, the RMS calculation accuracy of local wavefront measurements decreases as both t and RWR diminish. The variation in RWR has a more pronounced effect on the RMS calculation accuracy of the system's wavefront aberration compared to changes in t. When the misalignment of the secondary mirror is decentration or tilt and the width-to-radius ratio is $RWR \leq 0.5$, or when there is a misalignment in the Z direction between the secondary mirror and the primary mirror and the width-to-radius ratio is $RWR \leq 0.8$, the RMS accuracy of the local detection of the wavefront aberration of the system is much lower than that when the width-to-radius ratio is 1.

Therefore, our proposed method needs to be employed for the calibration of the optical system through local area detection and model comparison. When the misalignment of the secondary mirror is decentration or tilt and the width-to-radius ratio is RWR > 0.5, or when there is a misalignment in the Z direction between the secondary mirror and the primary mirror and the width-to-radius ratio is RWR > 0.8, the RMS accuracy of the local detection of the wavefront aberration of the system approaches the same accuracy as when the width-to-radius ratio is 1. Under these conditions, the RMS of the wavefront aberration in the central area of the detection system of the standard flat mirror can be calculated to guide the calibration of the optical system.

6. Conclusion

In this paper, we propose a new method for wave aberration detection in a 2-m ring ground-based solar telescope system. The detection model uses optical design software with the actual parameters of the 2 m ring primary mirror, the ring secondary mirror and the 1.6 m small-diameter standard flat mirror. We create a dataset of the variation in system wave aberration with the degree of misalignment of the secondary mirror. The wave aberration calculated by the detection model is compared with that detected using interferometer measurements to guide the calibration process. After the final local data splicing of the two sides, the wave aberration of the approximate full aperture is measured as PV $= 0.786\lambda$ and RMS $= 0.112\lambda$, which meets the high-precision requirements of solar observation. With the progress of solar observation technology, performance requirements of solar telescopes continue to increase, needing correspondingly higher resolution, better imaging quality and more stable observation capability. In future work, we will test the application of this method to larger-scale telescope projects, providing a clearer window for observing the Sun to obtain accurate solar data.

Acknowledgements

This work was supported by the Jiangsu Provincial Key Research and Development Program (BE2022072), the National Natural Science Foundation of China (12141304), and the Natural Science Foundation of Jiangsu Province (BK20231134).

Author Contributions

Renai Liu conceived the ideas, designed and implemented the study, and wrote the paper. Jinpeng Li delivered comprehensive guidance on simulation and experimentation, while also providing valuable recommendations for revision of the thesis. Zuozifei Song and Changyu Zeng revised the paper and improved quality of English. Yichun Dai provided assistance in the experiment. All authors read and approved the final manuscript.

Declaration of Interests

Jinpeng Li is the editorial board member for *Astronomical Techniques and Instruments* and he was not involved in the editorial review or the decision to publish this article. The authors declare no competing interests.

References

Wang, X. W., Yu, Y., Xu, Z. B., et al. 2023. Design and assessment of a micro-nano positioning hexapod platform with flexure hinges for large aperture telescopes. *Optics Express*, 31(3): 3908−3926.

Chesmore, G. E., Harrington, K., Sierra, C. E., et al. 2022. Characterizing the large aperture Simons observatory telescope receiver with radio holography. *Applied Optics*, 61(34): 10309−10319.

Meng, W. J., Xu, F. Y., Jin, Z. Y. 2024. New vacuum solar telescope achieves narrowband infrared solar imaging observation at He I 10830 Å. *Research in Astronomy and Astrophysics*, 24(5): 055008.

Arregui, I., Kolotkov, D., Nakariakov, V. M. 2023. Bayesian evidence for two slow-wave damping models in hot coronal loops. *Astronomy & Astrophysics*, 677: A23.

Savanov, I. 2023. The activity of a solar-type star TOI-1422 and mass loss of the atmosphere of the planet TOI-1422b. *Astronomy Reports*, 67(7): 719−724.

Jiang, Y. F., Zhan, J. Y., Yang, Y. L., et al. 2021. Investigations of sizes and dynamical motions of solar photospheric granules by a novel granular segmenting algorithm. *The Astrophysical Journal*, 923(2): 133.

Noda, C. Q., Schlichenmaier, R., Rubio, L. B., et al. 2022. The european solar telescope. *Astronomy & Astrophysics*, 666: A21.

Mathur, H., Thulasidharen, K., Pruthvi, H., et al. 2023. An image auto guider system for Kodaikanal Tower Tunnel Telescope. *Journal of Astronomical Instrumentation*, 12(2): 2350011.

Harrington, D. M., Sueoka, S. R., Schad, T. A., et al. 2023. Systems approach to polarization calibration for the Daniel K. Inouye Solar Telescope (DKIST). *Solar Physics*, 98(1): 10.

Rast, M. P., Bello Gonz´alez, N., Bellot Rubio, L., et al. 2021. Critical science plan for the Daniel K. Inouye solar telescope (DKIST). *Solar Physics*, 296(4): 70.

Liu, Z., Xu, J. 2011. 1-meter near-infrared solar telescope. In *Proceedings of First Asia-Pacific Solar Physics Meeting* ASI Conference Series.

Dai, Y. C., Liu, Z., Jin, Z. Y., et al. 2009. Active control of a 30 m ring interferometric telescope primary mirror. *Applied Optics*, 48(4): 664−671.

Cao, W., Gorceix, N., Coulter, R., et al. 2010. First light of the 1.6 meter off-axis New Solar Telescope at Big Bear Solar Observatory. *Astronomical Techniques and Instruments*, 2(3): 175—185.

Li, H. Z., Wang, Z., Wang, F., et al. 2012. Large diameter telescope wave aberration of outfield testing method. *Acta Photonica Sinica*, 41(1): 39—42. (in Chinese)

Li, B., Yuan, X. Y., Li, Z. Y., et al. 2021. Based on field star ellipticity of active collimating telescope method. *Acta Photonica Sinica*, 50(4): 226—235. (in Chinese)

An, Q., Zhang, H., Wang, K., et al. 2023. Photonics scanning pentaprism system for the integrated inspection of large-aperture telescopes. *Sensors*, 23(15): 6650.

Zhang, Y. Y., Wang, F. X., Xu, F. Y., et al. 2020. Development of inverted cone deflected thermal diaphragm for solar telescope. *Chinese Optics*, 13(3): 586—594. (in Chinese)

Rimmele, T. R., Warner, M., Keil, S. L., et al. 2020. The Daniel K. Inouye Solar Telescope-Observatory overview. *Solar Physics*, 295(12): 1—49.

Wang, K. Y., Dai, Y. C, Jin, Z. Y. 2022. Based on aberration detection solar telescope secondary posture correction methods. *Acta Photonica Sinica*, 51(6): 111—121. (in Chinese)

Liu, Z., Deng, Y. Y., Ji, H. S., et al. 2012. Chinese ground-based Large Solar Telescope. *Science in China: Physics, Mechanics, Astronomy*, 42(12): 1282—1291. (in Chinese)

Pan, S., Xu, X. F., Li, J. P., et al. 2020. Analysis of stray light in a 2 m ring ground-based solar telescope system. *Optical Instrument*, 42(3): 65—70. (in Chinese)

Figures

Source: ChinaXiv — Machine translation. Verify with original.

Figure 4: Figure 24